Universal nonlinear scattering in ultra-high Q whispering gallery-mode resonators

Guoping Lin,[1,2] Souleymane Diallo,[1] John M. Dudley,[1] and Yanne K. Chembo[1,*]

[1] *FEMTO-ST Institute [CNRS UMR6174], Optics Department, University Bourgogne Franche-Comté, 15B Avenue des Montboucons, 25030 Besançon cedex, France*

[2] *Now at MOE Key Laboratory of Fundamental Physical Quantities Measurement, School of Physics, Huazhong University of Science and Technology, 1037 Luoyu Road, Wuhan 430074, China*

**yanne.chembo@femto-st.fr*

Abstract: Universal nonlinear scattering processes such as Brillouin, Raman, and Kerr effects are fundamental light-matter interactions of particular theoretical and experimental importance. They originate from the interaction of a laser field with an optical medium at the lattice, molecular, and electronic scale, respectively. These nonlinear effects are generally observed and analyzed separately, because they do not often occur concomitantly. In this article, we report the simultaneous excitation of these three fundamental interactions in mm-size ultra-high Q whispering gallery mode resonators under continuous wave pumping. Universal nonlinear scattering is demonstrated in barium fluoride and strontium fluoride, separately. We further propose a unified theory based on a spatiotemporal formalism for the understanding of this phenomenology.

OCIS codes: (290.5900) Scattering, stimulated Brillouin; (290.5910) Scattering, stimulated Raman; (190.3270) Kerr effect; (190.4380) Nonlinear optics, four-wave mixing; (140.4780) Optical resonators.

References and links

1. R. W. Boyd, *Nonlinear Optics* (Academic, 2003).
2. G. P. Agrawal, *Nonlinear Fiber Optics, 5th ed.* (Academic, 2013).
3. J. M. Dudley, G. Genty, and S. Coen, "Supercontinuum generation in photonic crystal fiber," Rev. Mod. Phys. **78**, 1135 (2006).
4. S. K. Turitsyn, B. G. Bale, and M. P. Fedoruk,"Dispersion-managed solitons in fibre systems and lasers," Phys. Reports **521**, 135–203 (2012).
5. J. C. Beugnot, S. Lebrun, G. Pauliat, H. Maillotte, V. Laude, and T. Sylvestre, "Brillouin light scattering from surface acoustic waves in a subwavelength-diameter optical fibre," Nat. Commun. **5**, 5242 (2014).
6. J. M. Dudley, G. Genty, and S. Coen, "Enhancing and inhibiting stimulated Brillouin scattering in photonic integrated circuits," Nat. Commun. **6**, 6396 (2015).
7. H. Rong, R. Jones, A. Liu, O. Cohen, D. Hak, A. Fang, and M. Paniccia, "A continuous-wave Raman silicon laser," Nature **433**, 725–728 (2005).
8. I. V. Kabakova, R. Pant, D. Y. Choi, S. Debbarma, B. Luther-Davies, S. J. Madden, and B. J. Eggleton, "Narrow linewidth Brillouin laser based on chalcogenide photonic chip," Opt. Lett., **38**, 3208–3211 (2013).
9. D. J. Moss, R. Morandotti, A. L. Gaeta, and M. Lipson, "New CMOS-compatible platforms based on silicon nitride and Hydex for nonlinear optics," Nat. Photon. **7**, 597–607 (2013).
10. K. J. Vahala, "Optical microcavities," Nature **424**, 839–846 (2003).
11. A. Chiasera, Y. Dumeige, P. Feron, M. Ferrari, Y. Jestin, G. Nunzi Conti, S. Pelli, S. Soria, and G. C. Righini, "Spherical whispering-gallery-mode microresonators," Laser Phot. Rev. **4**, 457-482 (2010).

#262147 Received 29 Mar 2016; revised 4 May 2016; accepted 4 May 2016; published 22 Jun 2016

12. A. A. Savchenkov, A. B. Matsko, V. S. Ilchenko, and L. Maleki, "Optical resonators with ten million finesse," Opt. Express **15**, 6768–6773 (2007).
13. G. Lin, J. U. Fürst, D. V. Strekalov, and N. Yu, "Wide-range cyclic phase matching and second harmonic generation in whispering gallery resonators," Appl. Phys. Lett, **103**, 181107 (2013).
14. G. Lin and N. Yu, "Continuous tuning of double resonance-enhanced second harmonic generation in a dispersive dielectric resonator," Opt. Express **22**, 557–562 (2014).
15. A. A. Savchenkov, V. S. Ilchenko, F. Di Teodoro, P. M. Belden, W. T. Lotshaw, A. B. Matsko, and L. Maleki, "Generation of Kerr combs centered at 4.5 m in crystalline microresonators pumped with quantum-cascade lasers," Opt. Lett. **40**, 3468–3471(2015)
16. I. S. Grudinin, A. B. Matsko, and L. Maleki, "Brillouin lasing with a CaF_2 whispering gallery mode resonator," Phys. Rev. Lett. **102**, 043902 (2009).
17. M. Tomes and T. Carmon, "Photonic micro-electromechanical systems vibrating at *x*-band (11-ghz) rates," Phys. Rev. Lett. **102**, 113601 (2009).
18. J. Li, H. Lee, and K. J. Vahala, "Microwave synthesizer using an on-chip Brillouin oscillator," Nat. Commun. **4**, 2097 (2013).
19. G. Lin, S. Diallo, K. Saleh, R. Martinenghi, J.-C. Beugnot, T. Sylvestre, and Y. K. Chembo, "Cascaded Brillouin lasing in monolithic barium fluoride whispering gallery mode resonators," Appl. Phys. Lett. **105**, 231103 (2014).
20. C. Guo, K. Che, P. Zhang, J. Wu, Y. Huang, H. Xu, and Z. Cai, "Low-threshold stimulated Brillouin scattering in high-Q whispering gallery mode tellurite microspheres," Opt. Express **23**, 32261–32266 (2015).
21. W. Loh, A. A. Green, F. N. Baynes, D. C. Cole, F. J. Quinlan, H. Lee, K. J. Vahala, S. B. Papp, and S. A. Diddams, "Dual-microcavity narrow-linewidth Brillouin laser," Optica **2**, 225–232 (2015).
22. S. M. Spillane, T. J. Kippenberg,and K. J. Vahala, "Ultralow-threshold Raman laser using a spherical dielectric microcavity," Nature **415**, 621–623 (2002).
23. W. Liang, V. S. Ilchenko, A. A. Savchenkov, A. B. Matsko, D. Seidel, and L. Maleki, "Passively mode-locked Raman laser," Phys. Rev. Lett. **105**, 143903 (2010).
24. F. Vanier, M. Rochette, N. Godbout, and Y. A. Peter, "Raman lasing in As_2S_3 high-Q whispering gallery mode resonators." Opt. Lett. **38**, 4966–4969 (2013).
25. F. Daniele, B. Andrea, G. C. Righini, C. Gualtiero Nunzi, and S. Silvia, "Generation of hyper-parametric oscillations in silica microbubbles." Opt. Lett. **40**, 4508–4511 (2015).
26. B.-B. Li, W. R. Clements, X.-C. Yu, K. Shi, Q. Gong, and Y.-F. Xiao, "Single nanoparticle detection using split-mode microcavity Raman lasers," PNAS **111**, 14657-14662 (2014).
27. Ş. K. Özdemir, J. Zhu, X. Yang, B. Peng, H. Yilmaz, L. He, F. Monifi, S. H. Huang, G. L. Long, and L. Yang, "Highly sensitive detection of nanoparticles with a self-referenced and self-heterodyned whispering-gallery Raman microlaser," PNAS **111**, E3836–E3844 (2014).
28. T. J. Kippenberg, R. Holzwarth, and S. A. Diddams, "Microresonator-based optical frequency combs," Science **332**, 555–559 (2011).
29. Y. K. Chembo, D.V. Strekalov, and N. Yu, "Spectrum and dynamics of optical frequency combs generated with monolithic whispering gallery mode resonators," Phys. Rev. Lett. **104**, 103902 (2010).
30. A. A. Savchenkov, A. B. Matsko, W. Liang, V. S. Ilchenko, D. Seidel, and L. Maleki, "Kerr combs with selectable central frequency," Nat. Photon. **5**, 293–296 (2011).
31. A. Coillet, I. Balakireva, R. Henriet, K. Saleh, L. Larger, J. M. Dudley , C. R. Menyuk, snd Y. K. Chembo, "Azimuthal Turing patterns, bright and dark cavity solitons in Kerr combs generated with whispering-gallery-mode resonators," IEEE Photon. J. **5**, 6100409 (2013).
32. Y. K. Chembo and C. R. Menyuk, "Spatiotemporal Lugiato-Lefever formalism for Kerr-comb generation in whispering-gallery mode resonators," Phys. Rev. A **87**, 053852 (2013).
33. C. Godey, I. V. Balakireva, A. Coillet and Y. K. Chembo, "Stability analysis of the spatiotemporal Lugiato-Lefever model for Kerr optical frequency combs in the anomalous and normal dispersion regimes," Phys. Rev. A **89**, 063814 (2014).
34. A. Coillet and Y. K. Chembo, "Routes to spatiotemporal chaos in Kerr optical frequency combs," Chaos **24**, 013313 (2014).
35. A. Coillet and Y. K. Chembo, "On the robustness of phase-locking in Kerr optical frequency combs," Opt. Lett. **39**, 1529 (2014).
36. J. Pfeifle, A. Coillet, R. Henriet, K. Saleh, P. Schindler, C. Weimann, W. Freude, I. V. Balakireva, L. Larger, C. Koos, and Y. K. Chembo, "Optimally Coherent Kerr Combs Generated with Crystalline Whispering Gallery Mode Resonators for Ultrahigh Capacity Fiber Communications," Phys. Rev. Lett. **114**, 093902 (2015).
37. T. J. Kippenberg, S. M. Spillane, and K. J. Vahala,"Kerr-nonlinearity optical parametric oscillation in an ultrahigh-Q toroid microcavity," Phys. Rev. Lett. **93**, 083904 (2004)
38. A. A. Savchenkov, E. Rubiola, A. B. Matsko, V. S. Ilchenko, and L. Maleki, "Phase noise of whispering gallery photonic hyper-parametric microwave oscillators," Opt. Express **16**, 4130-4144 (2008).
39. W. Liang, A. B. Matsko, A. A. Savchenkov, V. S. Ilchenko, D. Seidel, and L. Maleki, "Generation of Kerr Combs in MgF_2 and CaF_2 Microresonators," in *Joint Conference of the IEEE International Frequency Control and the European Frequency and Time Forum (FCS) Proceedings* (IEEE, 2011), pp. 1–6 .

#262147 Received 29 Mar 2016; revised 4 May 2016; accepted 4 May 2016; published 22 Jun 2016

40. C. Milian, A. V. Gorbach, M. Taki, A. V. Yulin, and D. V. Skryabin, "Solitons and frequency combs in silica microring resonators: Interplay of the Raman and higher-order dispersion effects," Phys. Rev. A **92**, 033851 (2015).
41. Y. K. Chembo, I. S. Grudinin, and N. Yu, "Spatiotemporal dynamics of Kerr-Raman optical frequency combs," Phys. Rev. A **92**, 043818 (2015).
42. D. Farnesi, A. Barucci, G. Righini, S. Berneschi, S. Soria, and G. N. Conti, "Optical frequency conversion in silica-whispering-gallery-mode microspherical resonators," Phys. Rev. Lett. **112**, 093901 (2014).
43. W. Liang, A. A. Savchenkov, Z. Xie, J.F . McMillan, J. Burkhart, V. S. Ilchenko, C. W. Wong, A. B. Matsko, and L. Maleki, "Miniature multioctave light source based on a monolithic microcavity," Optica **2**, 40–47 (2014).
44. M. L. Gorodetsky and V. S. Ilchenko, "Optical microsphere resonators: optimal coupling to high-q whispering-gallery modes," J. Opt. Soc. Am. B **16**, 147–154 (1999).
45. G. Lin, S. Diallo, R. Henriet, M. Jacquot, and Y. K. Chembo, "Barium fluoride whispering-gallery-mode disk-resonator with one billion quality-factor," Opt. Lett. **39**, 6009–6012 (2014).
46. M. Laval, M. Moszyński, R. Allemand, E. Cormoreche, P. Guinet, R. Odru, and J. Vacher, "Barium fluoride-inorganic scintillator for subnanosecond timing," Nucl. Instr. Meth. Phys. Res.**206**, 169–176 (1983).
47. G. Lin and Y. K. Chembo, "On the dispersion management of fluorite whispering-gallery mode resonators for Kerr optical frequency comb generation in the telecom and mid-infrared range," Opt. Express **23**, 1594–1604 (2015).
48. A. A. Kaminskii, H. Rhee, H. J. Eichler, L. Bohatỳ, P. Becker, and K. Takaichi, "Wide-band Raman stokes and anti-stokes comb lasing in a BaF_2 single crystal under picosecond pumping," Laser Phys. Lett. **5**, 304–310 (2008).
49. R. Henriet, G. Lin, A. Coillet, M. Jacquot, L. Furfaro, L. Larger, and Y. K. Chembo, "Kerr optical frequency comb generation in strontium fluoride whispering-gallery mode resonators with billion quality factor," Opt. Lett. **40**, 1567–1570 (2015).
50. A. A. Kaminskii, L. Bohatỳ, P. Becker, H. J. Eichler, and H. Rhee, "Many-wavelength picosecond Raman Stokes and anti-Stokes comb lasing of cubic SrF_2 single crystal in the visible and near-IR," Laser Phys. Lett. **4**, 668–673 (2007).
51. M. J. Weber, *Handbook of Optical Materials* (CRC, 2002).
52. N. G. Broderick and S. X. Coen, "Analysis of cascaded Brillouin scattering in optical fibres," http://www.arxiv.org/abs/1504.04129.
53. I. H. Malitson, "Refractive properties of barium fluoride," J. Opt. Soc. Am. **54**, 628–632 (1964)
54. Y. K. Chembo and N. Yu, "Modal expansion approach to optical-frequency-comb generation with monolithic whispering-gallery-mode resonators," Phys. Rev. A **82**, 033801 (2010).
55. S. Schiller, "Asymptotic expansion of morphological resonance frequencies in Mie scattering," Appl. Opt. **32**, 2181–2185 (1993)
56. Y. K. Chembo, "Quantum dynamics of Kerr optical frequency combs below and above threshold: Spontaneous four-wave mixing, entanglement, and squeezed states of light," Phys. Rev. A **93**, 033820 (2016).

1. Introduction

Stimulated Brillouin, Raman and Kerr scattering are nonlinear optical processes that have been attracting great interest for decades [1, 2]. To enhance and observe these effects, tightly confined waveguide structures ranging from optical fibers to on-chip circuits have been used [3–6]. Further generation of stimulated Brillouin, Raman and Kerr scattering with relatively low pump power in the continuous-wave regime typically requires an optical cavity with small mode volume and ultra-high quality (Q) factor (that is, ultra-low loss). In this regard, cavity geometries based on chip-scale resonators have been demonstrated to be very successful solutions [7–9]. Another important platform has been the whispering gallery mode (WGM) cavity in which light is confined by successive total internal reflections at its inner circular interface. Such resonators are capable of featuring ultra-high Q factors in a very small mode volume [10, 11]. Mechanical polishing has been applied to utilize various crystalline materials, which lead to the recorded high Q-factors in the order of 10^{11} at 1.55 μm [12]. The main interest of such ultra-high Q resonators is that the long photon lifetime enhances the nonlinear effects, and enables to observe them with much smaller pump powers. This is why over the past few years, a plethora of ultra-high Q cavities made from nonlinear crystals have been demonstrated, even for applications into the ultraviolet and the mid-infrared frequency ranges [13–15].

Brillouin, Raman and Kerr scattering processes are schematically described in Fig. 1. Bril-

#262147 Received 29 Mar 2016; revised 4 May 2016; accepted 4 May 2016; published 22 Jun 2016

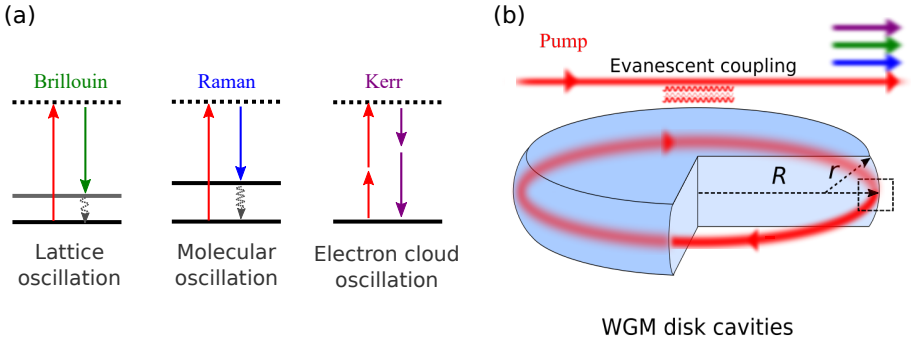

Fig. 1. Universal scattering behavior. (a) Simplified energy level scheme for Brillouin, Raman, and Kerr scattering. The excited states are virtual energy states. (b) The ultra-high Q resonator features a long photon lifetime ($\sim 1\ \mu$s) which increases the probability of occurrence for nonlinear interactions. Above a certain pump power threshold, these scattering effects become stimulated and can be steadily observed.

louin scattering corresponds to the interaction $\hbar\omega_p \rightarrow \hbar\omega_s + \hbar\Omega_B$, where a pump photon is scattered into a Stokes photon and an acoustical phonon (elastic lattice oscillation) whose frequency $\Omega_B/2\pi$ is generally of the order of 10 GHz [16–21]. On the other hand, Raman scattering obeys $\hbar\omega_p \rightarrow \hbar\omega_s + \hbar\Omega_R$ where the pump photon is downshifted to a Stokes photon after releasing an optical phonon (molecular vibration transition) with frequency $\Omega_R/2\pi \sim 10$ THz [22–27]. The Kerr effect relies on the four-wave mixing (FWM) interaction $\hbar\omega_\alpha + \hbar\omega_\beta \rightarrow \hbar\omega_\eta + \hbar\omega_\mu$, which is coherent and subjected to strict phase matching conditions [28–36]. This latter interaction is mediated by the quasi-instantaneous response of the electronic cloud of the lattice. In an ultra-high-Q WGM resonator with versatile transverse mode families, specific conditions can be found to combine different nonlinear effects in a single resonator. The coexistence and competition of Kerr and stimulated Raman scattering effects in WGM resonators have been studied by different groups [37,38]. The competition between Kerr frequency comb and both stimulated Brillouin and Raman scattering has also been discussed in calcium fluoride and magnesium fluoride resonators [39]. Although the coexistence of different effects are usually problematic, the combination of these effects can also be used in applications including new spectral components generation. To date, Kerr assisted Raman lasing, Raman assisted sum-frequency generation and hyperparametric oscillation have been realized and investigated [22, 23, 40–43].

In this article, we present the investigation of simultaneous excitation of Brillouin, Raman and Kerr effects in WGM cavities made from barium fluoride (BaF_2) and strontium fluoride (SrF_2) separately. So far, the very different multi-resonant and phase matching conditions required by Brillouin, Raman and Kerr interactions have made it difficult to excite them simultaneously, especially in the CW pump case. The specific advantage of monolithic WGM resonators is that their modal structure can allow to satisfy all these requirements at once. We show that crystalline WGM resonators therefore arise as ideal platforms in order to investigate the complex interplay of these three fundamental interactions, and we propose a full spatiotemporal model which provides an insightful understanding about these complex scattering phenomena.

2. Scheme and experimental setup

The scheme in Fig. 2(a) depicts the fulfillment of these conditions in the spectral domain. The gray peaks are the optical WGM resonances in the cavity. The red and green dashed curves present the Raman gain and the Brillouin gain, respectively. The Brillouin gain is one of the

#262147 Received 29 Mar 2016; revised 4 May 2016; accepted 4 May 2016; published 22 Jun 2016

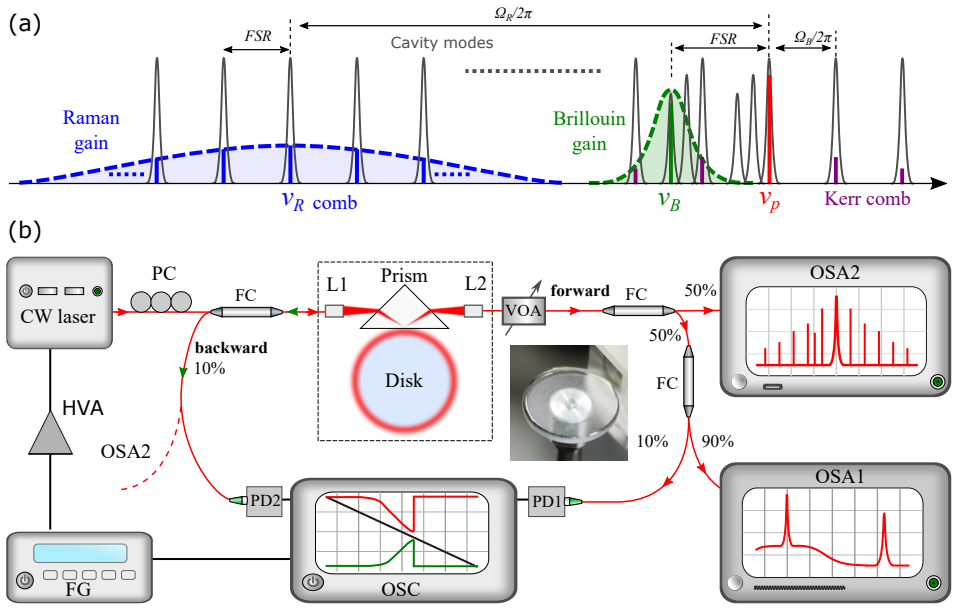

Fig. 2. Schematic illustration of the multi-resonant nonlinear optical frequency conversion and the experimental setup. (a) Schematic drawing of multi-resonant Raman, Brillouin, and Kerr combs in a monolithic optical cavity. FSR: free spectral range; Gray solid curves: cavity modes; Blue dashed curve: Raman gain; Green dashed curve: Brillouin gain; Red line: pump laser; Green solid line: Brillouin lasing; Blue solid lines: Raman lasing; Violet lines: Kerr comb. Note the overmoded nature of the WGM resonances allowed by the multiplicity of transverse mode families. (b) Scheme of the experimental setup. PC: fiber polarization controller; FC: fiber coupler; L1, L2: GRIN lenses; VOA: variable fiber optical attenuator; OSA1, OSA2: optical spectrum analyzers with 12.5 GHz and 0.1 GHz resolution, respectively; PD1, PD2: InGaAs photodetectors; FG: function generator; OSC: digital oscilloscope; HVA: high voltage amplifier. Inset: photo of the BaF_2 disk coupled by a prism.

strongest nonlinear gain but with a narrow bandwidth. It also has a relatively small frequency shift ω_B, typically in GHz level depending on the formation mechanism. On the other hand, the Raman gain is weaker, but it has a much larger frequency shift Ω_R and a wider gain bandwidth. These two parameters are linked to the elastic constants and molecule vibrations transitions. They are usually very different and dependent of the material itself. On the other hand, FWM processes are based on the Kerr nonlinearity and require strict phase matching condition. Considering WGMs in a cavity, this phase matching condition can be seen as the momentum conservation in the azimuthal mode indices. Therefore, the FWM comb usually occurs with a frequency spacing matching single or multiple free spectral range (FSR).

The experimental setup to observe these nonlinear effects is shown in Fig. 2(b). The pump source is a CW tunable laser with sub-kHz instantaneous linewidth at the wavelength of 1550 nm. The evanescent wave coupling technique was applied to efficiently excite the high Q factor WGMs in the monolithic disk cavity. In this experiment, a SF11 prism was used for the excitation of the modes in BaF2 disk. The pitailed gradient index (GRIN) lens L1 focused the incident pump light at the backside of the prism where total internal reflection occurs. The incident angle α was chosen such that it follows the phase matching condition $\alpha = \sin^{-1}(n_c/n_p)$ where n_c and n_p are the refractive indices of the cavity and the prism, respectively [44]. The

#262147 Received 29 Mar 2016; revised 4 May 2016; accepted 4 May 2016; published 22 Jun 2016

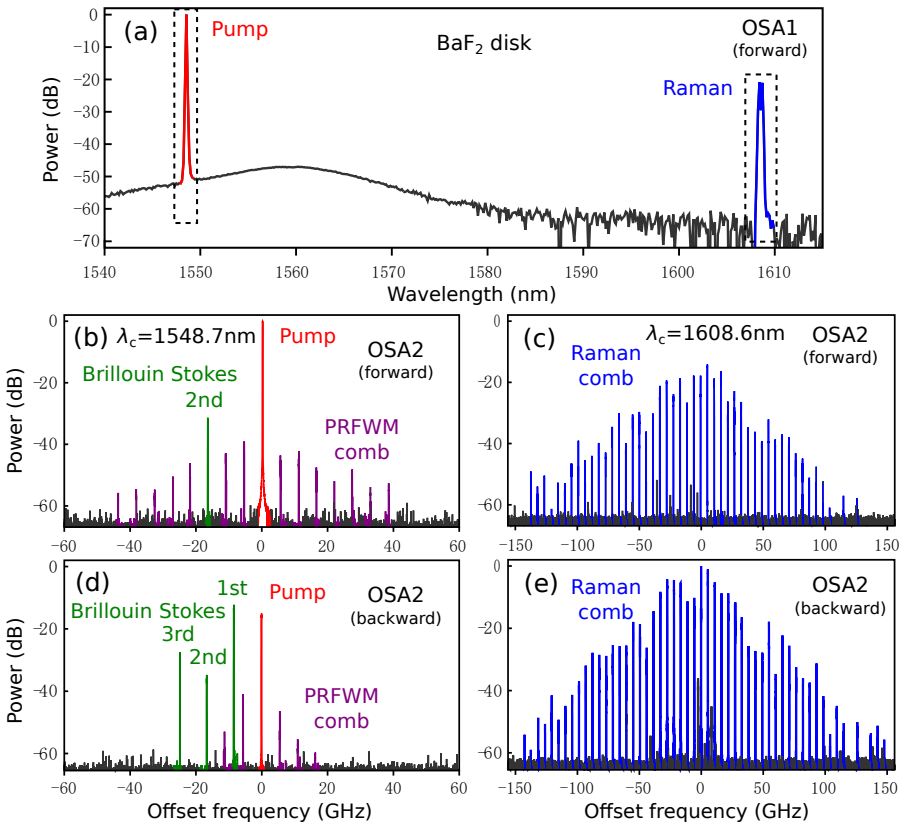

Fig. 3. Experimental optical spectra of Raman, Brillouin lasing and Kerr comb simultaneously observed in BaF_2. (a) Raman laser spectrum in the forward direction covering both the pump and Raman lasers in OSA1. The resolution is 0.1 nm. The measured Raman shift $\Omega_R/2\pi$ is equivalent to 240 cm^{-1}. (b,d) High resolution spectra in the forward and backward direction centered at the pump wavelength ($\lambda_c = 1548.7$ nm) in OSA2. The resolution is set at 0.1 GHz. The measured Brillouin shift $\Omega_B/2\pi$ is 8.3 GHz and the frequency spacing of the Kerr comb is 5.5 GHz. (c,e) High resolution spectra centered at the Raman wavelength ($\lambda_c = 1608.6$ nm) in OSA2. The frequency spacing of the Raman comb is 5.5 GHz.

reflected light from the prism was then collected into a single mode fiber using the lens L2. The measured coupling efficiency is up to 70% when the reflected light was directly focused on a photodetector. The coupling from the incident fiber to the output one is about 70%. A fiber polarization controller optimized the incident light for the WGM excitation. The output light was attenuated using a variable fiber optical attenuator (VOA). The 50/50 fiber coupler (FC) and the 10/90 one split the output light separately into a photodetector PD1, a fiber spectrum analyzer OSA1 with the resolution down to 0.1 nm (or 12.5 GHz) and a high resolution one OSA2 (APEX OSA) with a resolution down to 10 MHz. The laser frequency was ramped by a amplified triangle wave to scan across the selected WGM during the measurement. Another fiber direction coupler inserted before L1 then directed 10% of the feedback light in the backward direction into the photodetector PD2 or the high resolution spectrum analyzer OSA2.

#262147 Received 29 Mar 2016; revised 4 May 2016; accepted 4 May 2016; published 22 Jun 2016

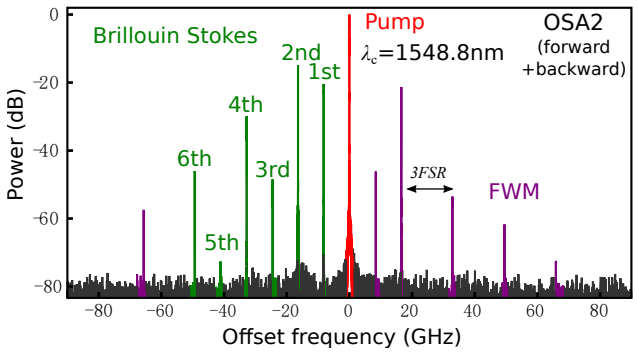

Fig. 4. Experimental Brillouin spectra with FWM peaks in BaF_2. No odd order anti-Stokes peaks were observed in both forward and backward direction. The measured frequency spacing between the even order Stokes is 16.5 GHz, matching the triple FSR value.

3. Experimental results: universal nonlinear scattering in barium fluoride

Monolithic crystalline optical cavities made of BaF_2 with Q factors up to one billion has been recently demonstrated [45]. BaF_2 is a very interesting material due to its scintillation feature for high energy particle detection [46] and its very low anomalous material dispersion in the mid-infrared light regime for potential Kerr frequency comb generation [47]. As it has a refractive index of 1.466 at 1550 nm, larger than that of an optical fiber. The prism coupling method using SF11 glass was used to excite high-Q WGMs in BaF_2 cavities as shown in Fig. 2(b). The incident power at the input port was first set at 100 mW for the pumping.

Figure 3(a) presents an optical spectrum covering the spectral range from 1540 to 1615 nm. A new wavelength peak was observed at 1608.6 nm. The measured frequency shift in wavenumber ($\Delta\Omega_R$) is 240 cm^{-1}, which is in good agreement with the known Raman shift of about 238 cm^{-1} [48]. To further explore the spectral components in detail, a branch of the output light was also monitored by the OSA2 with a high resolution set at 100 MHz as shown in Fig. 3(b,c). One can notify a comb with frequency spacing of 5.5 GHz around the pump wavelength and a multiwavelength Raman laser with the same frequency spacing. Compared with the known Kerr optical frequency comb [28], the observed comb lines around the pump wavelength are always accompanied by the Raman comb. Thereby, we conclude that these new frequency components around the pump wavelength result from the FWM process between the pump laser and the Raman comb laser, as also reported in silica cavities [22, 41]. Moreover, one can clearly see a strong peak around the pump wavelength. It is separated from the pump by 16.6 GHz that is about twice of the calculated Brillouin shift of 8.27 GHz for BaF_2 [19]. To further investigate this peak, we have studied the optical spectra of the feedback light in the backward direction as shown in Fig. 3 (d,e). Clear cascaded Brillouin lasing peaks from the first to the third Stokes are recognized around the pump wavelength. It should be mentioned that the cavity enhanced universal nonlinear scattering depends strongly on the resonance structures, it is also possible to harvest these lasers independently by choosing a proper mode and controlling its coupling strength. For instance, single Brillouin lasing was demonstrated in a BaF_2 disk [19].

We also report here the observation of FWM between the pump and the even order Brillouin Stokes. It is known that FWM requires a strict phase matching condition. It is usually fulfilled by involving equally spaced modes in the same azimuthal family, leading to single or multiple FSR spacing. In a BaF_2 cavity with a diameter of 11.87 mm, the corresponding FSR is 5.5 GHz calculated using the formula $FSR = c/(\pi n_g d)$ where c is the speed of light in vacuum, n_g is the group velocity index and d is the diameter of the disk. The triple FSR value coincides with

#262147 Received 29 Mar 2016; revised 4 May 2016; accepted 4 May 2016; published 22 Jun 2016

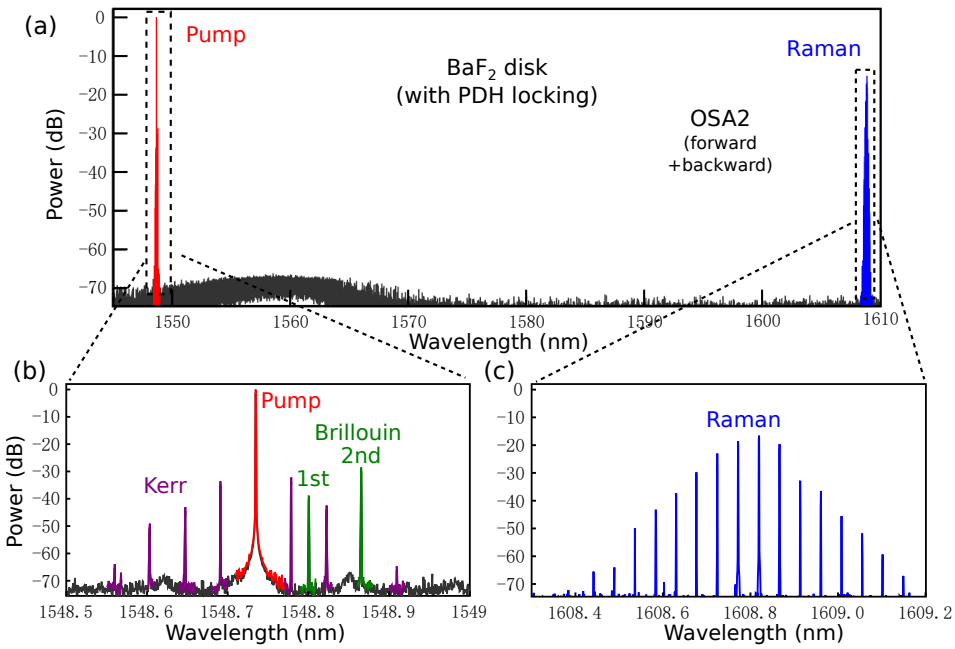

Fig. 5. Experimental optical spectra of Raman, Brillouin lasing and Kerr comb simultaneously observed in BaF_2 with PDH locking implemented. Note: time scale is shown in wavelength.. (a) Full spectrum covering both the pump and Raman signals. (b,c) The corresponding zoom-in spectra.

the twice value of the Brillouin shift. Therefore, by choosing specific WGMs in an optimized coupling condition, we are able to observe the FWM between the pump and the even order Brillouin Stokes as shown in Fig. 4.

We further implemented the Pound-Drever-Hall (PDH) technique in order to lock the pump laser frequency to the selected WGM resonance. A 2×2 fiber coupler was used to combine both the forward and backward beams. The attenuator was adjusted such that the power is balanced in both directions. We were able to record the spectra of the universal scattering with lower pump power as shown in Fig. 5. It is however important to note that the Raman coupling between the modes around the pump and those around the 1st Stokes line is incoherent; however, the group of modes for the first Raman Stokes line is mainly phase-locked because they are strongly coupled by the coherent Kerr-induced FWM [23]. At the experimental level, the coherence of the Brillouin and Raman combs can be monitored after separate photodetection through the linewidth of the corresponding beatnotes. Figure 6 shows the the examples of beatnotes obtained in BaF_2 disk resonators. It can be seen that the 20-dB linewidth of these beatnotes is in the kHz range. It is expected that the largest part of this linewidth originates from noise, and that further improvement of the phase-locking technique and optimization of the mode coupling conditions would significantly improve this spectral purity.

Figure 7 shows the typical temporal response observed for the transmitted and reflected signals as the pump is detuned across the resonance.

#262147 Received 29 Mar 2016; revised 4 May 2016; accepted 4 May 2016; published 22 Jun 2016

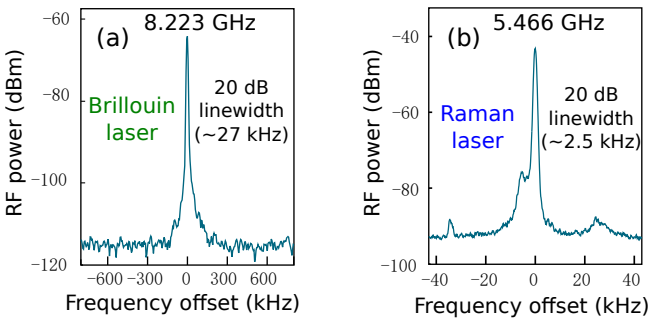

Fig. 6. Beatnote spectra for Raman and Brillouin lasing. (a) Brillouin lasing. The beatnote has the Brillouin shift frequency (8.223 GHz). (b) Raman lasing. The beatnote has the FSR frequency (5.466 GHz).

4. Experimental results: universal nonlinear scattering in strontium fluoride

To further investigate the cm-size WGM cavity as a versatile optical platform for simultaneously inducing Brillouin, Raman lasers and Kerr combs, we have also investigated a handily polished cavity made from a 1.2 cm diameter SrF_2 disk preform. As SrF_2 has a refractive index of 1.430 slightly smaller than that of silica fiber, a low loss tapered microfiber is sufficient to excite the high-Q WGMs [49]. Figure 8 shows the experimental observed optical spectra in SrF_2. During the measurement, the fiber taper was put in contact with the cavity. An incident laser at 1548.7 nm with 40 mW was launched through the tapered fiber coupler. Similar to BaF_2, the laser frequency was kept scanning across a selected mode for pumping. In the OSA1, one can clearly see the Raman lasing in the SrF_2 cavity. The measured Raman shift of 283 cm^{-1} matches the reported value [50]. Due to the fact that the Raman laser at 1619.7 nm is outside the measurable spectral range of the OSA2, we hereby only present the high resolution spectra obtained by the OSA2 around the pump wavelength.

Figure 8(b) shows the optical spectrum in the forward direction. Similar to BaF_2, we also observe a comb with frequency spacing of 6.1 GHz that is one FSR of the cavity. As it occurs with the Raman laser, it is a signature of Raman assisted FWM. Besides, one notifies a new spectral component with an offset of 9.8 GHz from the pump laser. To understand this peaks, we have carried out the calculation of backscattered Brillouin shift that usually results from the interaction between the intracavity light and the longitudinal acoustic wave in fluoride cavities [16]. This value can be expressed as [1]: $\Omega_B/2\pi = 2n_{\text{eff}}V_a/\lambda_p$ where n_{eff} is the effective refractive index of the optical mode, λ_p is the pump wavelength in vacuum, and V_a is the longitudinal acoustic wave speed. The last one can be calculated using $V_a = [(C_{11}+C_{12}+2C_{44})/(2\rho)]^{1/2}$, with C_{11}, C_{12}, C_{44} being three independent elastic constants and ρ the material density. These values in SrF_2 are $\{1.2350, 0.4305, 0.3128\} \times 10^{11}$ $N.m^{-2}$ and 4.24 $g.cm^{-3}$, respectively [51]. This yields a sound speed of $V_a = 5.20$ $km.s^{-1}$. Considering the material refractive index of 1.430 at 1548.7 nm, we find a Brillouin shift $\Omega_B/2\pi = 9.60$ GHz, which is close to the value we measured. The observation of this peak in the forward direction comes from the Rayleigh scattering induced feedback in the cavity. Figure 8(c) further verify the observed Brillouin laser in the backward direction. However, we do not observe the second Brillouin Stokes. This could be due to the fact that no strong resonance exits in the second Stokes position. Beside the first Brillouin Stoke, more complicated spectral components are present in the backward direction. Nevertheless, it can be seen as two independent one-FSR spaced combs around the Brillouin Stokes and an anti-Stokes (colored in black). These combs are the FWM products of the Brillouin lasers and the corresponding Raman combs, as referred to BRFWM. The observation

#262147 Received 29 Mar 2016; revised 4 May 2016; accepted 4 May 2016; published 22 Jun 2016

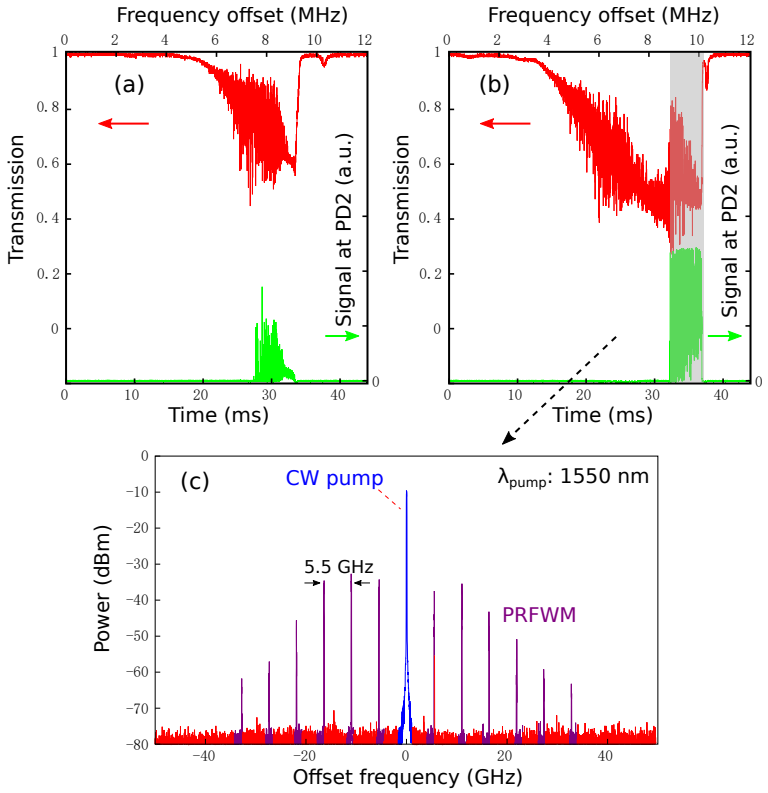

Fig. 7. Observation of a mode transition related to the FWM between the pump and the Raman comb. (a), (b) Red curves: transmission of the pump light through the prism coupling setup. Green curves: detected signal in the backward direction in PD2. The coupling strength is increased in (b) by decreasing the coupling gap between the prism and the cavity. Gray regime highlights a transition regime which is accompanied with the observation of a FWM comb. (c) Typical FWM comb spectrum.

of complex spectra with a lower pump in SrF_2 could result from its much smaller material dispersion when compared with BaF_2.

5. Theoretical analysis and numerical simulations

The Brillouin, Raman and Kerr effects result from the interaction between the pump field and the crystals of interest at the lattice, molecular and electronic scale, respectively. A unified description of the simultaneous excitation of these three scattering behaviours requires taking into account the very wide diversity of time-scales and nonlinear interactions involved for each effect. For example, a dynamical description of Brillouin scattering has to involve coupled equations for the intra-cavity backward and forward fields, and for the azimuthal acoustic field which is mediating the phonon-photon interaction. A spatiotemporal model for Raman scattering in WGM resonators needs to incorporate all-order dispersion since the optical phonons are scattered several tens of THz away from the pump; Spatiotemporal models for Kerr combs have already been provided in the literature under the form of a generalized Lugiato-Lefever equation (or LLE). From a theoretical viewpoint, our spatiotemporal model will therefore consist in generalizing the LLE to include Raman scattering (forward field $\mathscr{E}$), and in coupling this equation to both the multimode backward field $\mathscr{B}$, and in providing a dynamical equation for

#262147 Received 29 Mar 2016; revised 4 May 2016; accepted 4 May 2016; published 22 Jun 2016

acoustical phonon field $\mathscr{S}$ which couples the contra-propagating multimode fields $\mathscr{E}$ and $\mathscr{B}$. An important challenge is to provide here a consistent theoretically model which accounts for the fact that experimentally, the forward field $\mathscr{E}$ and the Brillouin-induced backward field $\mathscr{B}$ do propagate in different transverse mode families (see Fig. 1), which are coupled by the phonon field $\mathscr{S}$. The three fields of interest in the cavity can be expanded in the moving frame as

$$\mathscr{E}(\theta,t) = \sum_{l=-N}^{N} \mathscr{E}_l(t)\, e^{il\theta} \tag{1}$$

$$\mathscr{B}(\theta,t) = \sum_{l=-N}^{0} \mathscr{B}_{3(l-\frac{1}{2})}(t)\, e^{i3(l-\frac{1}{2})\theta} \tag{2}$$

$$\mathscr{S}(\theta,t) = \mathscr{Q}(t)\, e^{i\frac{3}{2}\theta} + \mathscr{R}^*(t)\, e^{-i\frac{3}{2}\theta} \tag{3}$$

where t is the time, $\theta \in [-\pi,\pi]$ is the azimuthal angle along the rim of the disk, $\mathscr{E}_n(t)$ and $\mathscr{B}_n(t)$ are the slowly-varying amplitudes of the forward and backward optical fields, which are $n\Omega_{\text{FSR}}$-shifted with regards to the pump (n being integer or half-integer). The variables $\mathscr{Q}$ and $\mathscr{R}$ are the slowly-varying amplitudes of the forward and backward acoustic phonon fields [2, 52] with a Brillouin shift $\Omega_B = \frac{3}{2}\Omega_{\text{FSR}}$.

The spatiotemporal dynamics of the intracavity fields is explicitly written as

$$\begin{aligned}\frac{\partial \mathscr{E}}{\partial t} &= -\kappa\mathscr{E} + i\sigma_{\text{e}}\mathscr{E} + iv_g\hat{\text{D}}_\theta\,\mathscr{E} + \sqrt{2\kappa_{\text{ext}}/T_{\text{FSR}}}\,\sqrt{P_{\text{L}}} \\ &\quad + iv_g\gamma f_{\text{R}}\left[\mathscr{E}(\theta,t)\int_{-\pi}^{\pi} \text{h}_{\text{R}}(\theta'/\Omega_{\text{FSR}})|\mathscr{E}(\theta-\theta',t)|^2 d\theta'\right] \\ &\quad + iv_g\gamma(1-f_{\text{R}})[|\mathscr{E}|^2 + 2|\mathscr{B}|^2]\mathscr{E} + iv_g\eta\,\mathscr{B}\mathscr{S} \end{aligned} \tag{4}$$

$$\frac{\partial \mathscr{B}}{\partial t} = -\kappa\mathscr{B} + i\sigma_{\text{b}}\mathscr{B} + iv_g\gamma[|\mathscr{B}|^2 + 2|\mathscr{E}|^2]\mathscr{B} + iv_g\eta\,\mathscr{E}\mathscr{S}^* \tag{5}$$

$$\frac{\partial \mathscr{S}}{\partial t} = -\mu\mathscr{S} + i\mu\{\langle\mathscr{B}e^{i\frac{3}{2}\theta}|\mathscr{E}\rangle e^{i\frac{3}{2}\theta} + \langle\mathscr{B}|\mathscr{E}e^{i\frac{3}{2}\theta}\rangle e^{-i\frac{3}{2}\theta}\}. \tag{6}$$

Equation (4) governs the dynamics of the forward optical field, and the first term in the right-hand side (RHS) describes the total (intrinsic and extrinsic) losses, characterized by the full-linewidth $2\kappa = \omega_{\text{C}}/Q_{\text{tot}}$, where Q_{tot} is the loaded quality factor. The second term accounts for the effect of the off-resonance pumping, with $\sigma_{\text{e}} = \omega_{\text{L}} - \omega_{\text{C}}$ being the laser frequency detuning with respect to cold-cavity resonance of the pumped mode. The third term includes both the material and geometrical dispersion at all orders through the dispersion operator

$$\hat{\text{D}}_\theta \equiv \sum_{k=2}^{+\infty} (i\Omega_{\text{FSR}})^k(\beta_k/k!)\,\partial_\theta^k, \tag{7}$$

where the β_k are dispersion coefficients. The fourth term accounts for the external pumping term, which depends on the coupling full-linewidth $2\kappa_{\text{ext}}$, on the intra-cavity round-trip time $T_{\text{FSR}} = 2\pi/\Omega_{\text{FSR}}$, and on the optical pump power P_{L}. The fifth and sixth terms describe the Raman and Kerr effects (self- and cross-phase modulation), respectively. The strength of these $\chi^{(3)}$ nonlinearities is proportional to the coefficient $\gamma = \omega_{\text{L}} n_2/cA_{\text{eff}}$, where n_2 is the nonlinear optical coefficient, and $A_{\text{eff}} \sim \lambda_{\text{L}}^{\frac{7}{6}} a^{\frac{5}{6}}$ is the effective mode area. The spectro-temporal behavior of the Raman induced-fields is governed by the impulse response $\text{h}_{\text{R}}(t)$ which accounts for the delayed molecular response of the crystals, and its strength is also proportional to the Raman fractional response f_{R}. The seventh and last term accounts for the Brillouin interaction with the backwards and acoustic fields. The coupling parameter is $\eta = g_B/2A_{\text{eff}}$ where g_B is the usual Brillouin gain in units of m/W. Equation (5) describes the dynamics of the backward

#262147 Received 29 Mar 2016; revised 4 May 2016; accepted 4 May 2016; published 22 Jun 2016

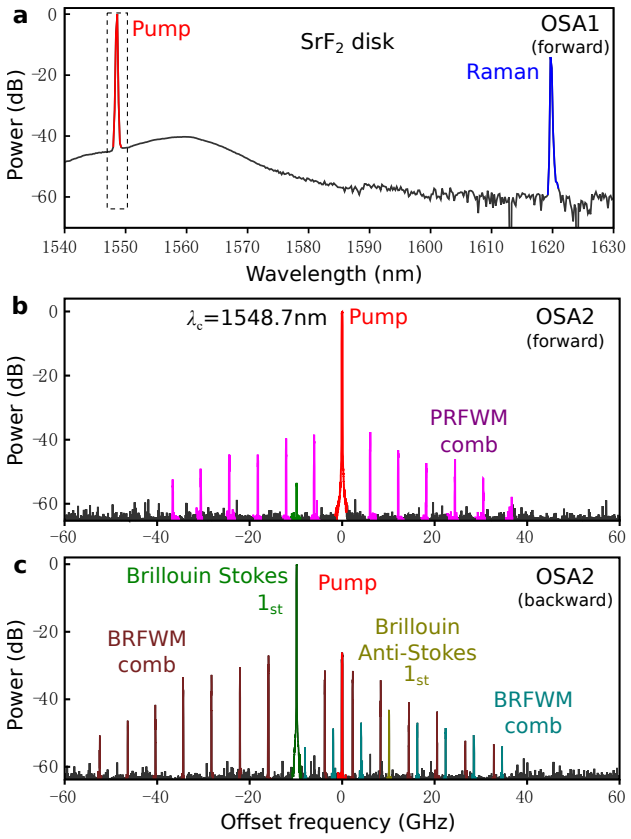

Fig. 8. Experimental optical spectra of Raman, Brillouin lasing and FWM comb simultaneously observed in SrF_2. (a) Raman laser spectrum in the forward direction covering both the pump and Raman lasers in OSA1. The resolution is 0.2 nm. The Raman laser occurs at 1619.7 nm, outside the measurable range of OSA2. The measured Raman shift $\Omega_R/2\pi$ is 283 cm^{-1}. (b) High resolution spectra in the forward direction centered at the pump wavelength ($\lambda_c = 1548.7$ nm) in OSA2. The resolution is set at 0.1 GHz. The measured Brillouin shift $\Omega_B/2\pi$ is 9.8 GHz and the frequency spacing of the PRFWM comb *FSR* is 6.1 GHz. (c) High resolution spectra in the backward direction centered at the pump wavelength ($\lambda_c = 1548.7$ nm) in OSA2. The measured frequency spacing of two BRFWM combs is 6.1 GHz.

optical field, which is subjected to linear losses, cavity detuning and Brillouin gain. Finally, the dynamics of the acoustic field is ruled by Eq. (6). The acoustic losses are characterized by the phonon lifetime $\tau_B = 1/2\mu$, and this phonon field is excited by the optical fields $\mathscr{E}$ and $\mathscr{B}$ through quadratic inner product terms of the kind

$$\langle \mathscr{M} | \mathscr{N} \rangle = \frac{1}{2\pi} \int_{-\pi}^{+\pi} \mathscr{M}^* \mathscr{N} \, d\theta \,. \tag{8}$$

For the sake of simplicity, we have only included in Eqs. (4)-(6) the core ingredients needed to understand essential physical interactions between Brillouin, Raman and Kerr nonlinearities. We have for example omitted some marginal features like acoustic field detuning and spatial dynamics, effect of the backward field on Raman scattering, or imperfect overlap between the different families of transverse modes.

#262147 Received 29 Mar 2016; revised 4 May 2016; accepted 4 May 2016; published 22 Jun 2016

Table 1. Coefficents of the Sellmeier equation $n^2(\lambda) = 1 + \sum_{i=1}^{3} A_i \lambda^2/(\lambda^2 - \lambda_i^2)$ for barium and strontium fluoride, with λ in units of μm [51, 53].

Coefficients A_i and λ_i	BaF_2	SrF_2
A_1	0.643356	0.67805894
A_2	0.506762	0.37140533
A_3	3.8261	3.8484723
λ_1	0.057789	0.05628989
λ_2	0.10968	0.10801027
λ_3	46.3864	34.649040

Here we further discuss the determination of the overall dispersion at all orders. Complete accounting for higher-order dispersion coefficients β_k becomes here mandatory because the Raman gain is shifted up to multiple tens of THz away from the pump. The determination of all-order dispersion is very well documented in the literature when only the chromatic contribution is accounted for (see [2, 3] and references therein). We explain below how to include geometrical dispersion as well in the case of our disk-resonators. All-order dispersion is accounted for through the operator $\hat{\mathsf{D}}_\theta \equiv \hat{\mathsf{D}}_{\mathsf{chr}} + \hat{\mathsf{D}}_{\mathsf{geo}}$ which yields a dispersion profile in the Fourier-domain, with

$$\tilde{\mathsf{D}}_{\mathsf{chr}}(\omega) = \frac{1}{c}[\omega n(\omega) - \omega_{\mathrm{L}} n(\omega_{\mathrm{L}})] - \beta_{1,\mathsf{chr}}(\omega - \omega_{\mathrm{L}}), \tag{9}$$

and

$$\tilde{\mathsf{D}}_{\mathsf{geo}}(\omega) = -\frac{\xi_q}{2^{1/3} a}\left\{\left(\frac{\omega}{\Omega_{\mathrm{FSR}}}\right)^{1/3} - \left(\frac{\omega_{\mathrm{L}}}{\Omega_{\mathrm{FSR}}}\right)^{1/3} - \frac{1}{3}\left(\frac{\omega_{\mathrm{L}}}{\Omega_{\mathrm{FSR}}}\right)^{1/3}\frac{(\omega - \omega_{\mathrm{L}})}{\omega_{\mathrm{L}}}\right\} \tag{10}$$

being respectively the chromatic and geometrical contributions to dispersion, where $\beta_{1,\mathsf{chr}} = \partial_\omega[\omega n(\omega)/c]_{\omega_{\mathrm{L}}}$, where ω_{L} is the laser angular frequency. The chromatic dispersion can be accurately determined using the Sellmeier expansion of $n(\omega)$ (see Table 1), while the contribution of geometrical dispersion can be calculated from the approximation of spherical resonators [55], which is accurate for disk-resonators with curvature radii significantly larger than the pump wavelength, with ξ_q being the q^{th} root of the Airy function $\mathrm{Ai}(-z)$ for eigenmodes in the q^{th} radial family.

In the present work, we model the Raman gain $g(\Omega)$ as a Lorentzian lineshape of peak value g_{R}, center frequency Ω_{R} and FWHM linewidth $\Delta\Omega_{\mathrm{R}}$. Hence, the fractional impulse and the fractional coefficient can be respectively expressed as

$$\mathrm{h_R}(t) = \mathrm{H}(t)\,\frac{\tau_1^2 + \tau_2^2}{\tau_1 \tau_2^2}\, e^{t/\tau_2} \sin(t/\tau_1) \tag{11}$$

$$f_{\mathrm{R}} = \frac{c}{\pi \omega_{\mathrm{L}} n_2(\omega_{\mathrm{L}})} \int_0^{+\infty} dt \int_0^{+\infty} d\Omega\, g(\Omega) \sin(\Omega t), \tag{12}$$

where $\tau_1 = 1/\Omega_{\mathrm{R}}$, $\tau_2 = 2/\Delta\Omega_{\mathrm{R}}$, and $\mathrm{H}(t)$ is the Heaviside step function, and n_2 is the nonlinear coefficient at ω_{L} [2]. It is important to note that even though the fractional impulse function is generally written as a function of (the so-called *fast*) time, it can easily be written as a function

#262147 Received 29 Mar 2016; revised 4 May 2016; accepted 4 May 2016; published 22 Jun 2016

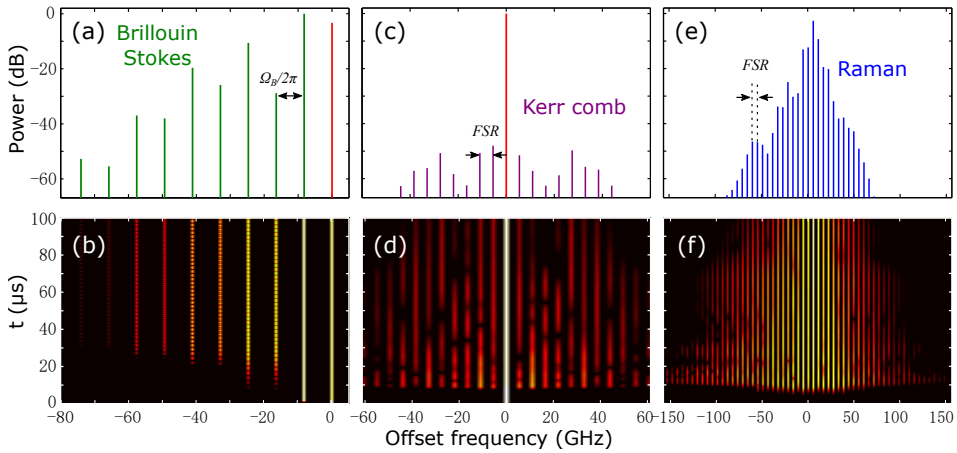

Fig. 9. Numerical simulations for a BaF_2 disk-resonator. The parameters are set to $\gamma = 1$ W^{-1}km^{-1}, and $\kappa/2\pi = 1.2$ MHz, $\kappa_{ext}/2\pi = 0.8$ MHz. (a) Brillouin power spectrum around the pump. Note that the intermodal spacing corresponds to the Brillouin frequency shift. (b) Corresponding spectro-temporal dynamics. (c) Kerr-induced four-wave mixing around the pump. (d) Corresponding spectro-temporal dynamics. (e) Power spectrum around the first Raman Stokes line. (f) Corresponding spectro-temporal dynamics.

of the azimuthal angle θ through the formal transformation $t \rightarrow \theta/\Omega_{FSR}$. Accordingly, the convolution integral from $\pm\infty$ can now be performed with regards to θ from $\pm\pi$, provided that the exponential decay time τ_2 (inverse of the Raman gain linewidth) is significantly smaller than the round-trip time of the resonator (in other words, the oscillations $h_R(t)$ have to fit within one round-trip time $T_{FSR} = 2\pi/\Omega_{FSR}$). As a consequence, this model is valid for large resonators (for which $\Omega_{FSR} \ll \Omega_R$, that is $d \gg v_g\tau_2$, with $v_g = c/n_g$), but not for small ones such as microring resonators.

The simultaneous generation of Brillouin, Raman and Kerr scattering can be analyzed after simulating Eqs. (4)-(6), as presented in Fig. 9. The model enables to track the instantaneous spectro- and spatio-temporal dynamics of the optical and acoustic intracavity fields. Figures 9(a) and (b) display the sequential birth of the Stokes and anti-Stokes Brillouin lines, which are separated with a frequency Ω_B. On Figs 9(c) and (d), the spectral lines excited by the Kerr-induced FWM are displayed. These lines clearly have an non-stationary behavior because they are dynamically coupled to the Raman lines displayed in Figs. 9(e) and (f). It is noteworthy that our model replicates all the main features of the experimental data in terms of relative amplitudes, frequency shifts and stability of the oscillating modes.

6. Conclusion

In conclusion, we have reported the simultaneous excitation of Brillouin, Raman and Kerr effects in cm-scale ultra-high Q WGM crystalline resonators fabricated with barium fluoride. The present research shows that the cm-size monolithic cavity platform can be used to induce multi-resonant enhanced nonlinear optical effects with a relatively low power CW laser. The cm-size disks feature FSR of the same order of magnitude as the Brillouin frequency shift. Together with rich multimode structures, they favor the fulfillment of experimental conditions for co-excitation of universal nonlinear effects in one single resonator. We have also developed a spatiotemporal model which has enabled us to understand theoretically this complex lasing behavior, which involves light-matter interactions at lattice, molecular and electronic

#262147 Received 29 Mar 2016; revised 4 May 2016; accepted 4 May 2016; published 22 Jun 2016

scales. It is also an excellent method to implement a strategy to suppress undesirable effects if needed (by frustrating some transverse mode interactions, tuning appropriately the pump laser frequency/power, etc.) From a broader viewpoint, our study provides unambiguous evidence that ultra-high Q WGM resonators can host simultaneous nonlinear frequency conversion processes in different materials, and that the corresponding output signal can be harvested for a wide range of applications including sensors, telecommunications and all-optical information processing, and quantum information [56].

Acknowledgments

Y. K. C. acknowledges support from the European Research Council (ERC) through the projects NextPhase (StG 278616) & Versyt (PoC 632108), from the *Centre National d'Etudes Spatiales* (CNES) through the project SHYRO, from the *Région de Franche-Comté* through the project CORPS, and from the Labex ACTION.

#262147 Received 29 Mar 2016; revised 4 May 2016; accepted 4 May 2016; published 22 Jun 2016